RESEARCH ARTICLE

Finite Element Modeling and Experimental Validation of a z-Type Self-Expanding Endovascular Stent

Joel C. R. Scott[a] and Darrel A. Doman[a] and Clifton R. Johnston[a]

[a]Department of Mechanical Engineering Dalhousie University, C360 - 5269 Morris Street (Sexton Campus), PO Box 15000, B3H 4R2, Halifax, NS, Canada

ARTICLE HISTORY
Compiled June 30, 2021

ABSTRACT
Stent migration due to haemodynamic drag remains the primary cause of type I endoleak, potentially leading to aneurysm rupture. The prevalence of migration and endoleak can be partially attributed to deficiencies in stent-graft radial spring design and a lack in understanding of the mechanical properties of endovascular stents. A converged finite element model of a custom radial extensometer was developed, fit, and validated using experimental results for bare stent wire ("uncovered") with outer diameter of 12 mm stent. During stent constriction to 50 % of the original cross-sectional area, a comparison of experimental and modeled results produced an r^2 value of 0.946, a standard error of 0.099 N, and a mean percent error of 1.69 %. This validated finite element model can be used to analyze the mechanisms responsible for radial force generation in 316L stainless steel self-expanding endovascular stents, as well as to evaluate new stent designs.

1. Introduction

In this study we will present a complete dynamic finite element model (FEM) of the compression and expansion of a z-type endovascular stent. This model mimics the function of a novel radial extensometer, and is intended as a tool for both investigating the mechanical function of 316L Stainless Steel (SS) self-expanding stents, and aiding in the efficient design of new prosthetics. Validated against real-world data, this model was developed in the hopes of investigating various different scenarios including but not limited to: the mechanical systems responsible for stent radial force generation, the conversion of radial force to the linear force measured by the radial extensometer force gauge, the impact of geometrical and mechanical design changes on stent performance, as well as for simulating novel stent designs.

Developing the ability to manipulate the fixation (radial) force to an ideal value for each individual stent and patient has the potential to improve the short and long-term success rate of endovascular aneurysm repair (EVAR).

The design of endovascular devices has progressed for years using a trial and error methodology focused on experimental testing, however, computational design has seen a relatively slow adoption in medical device design[1, 2]. Aside from change in radial force and stent properties due to stress-induced transformation of austenite to martensite in super-elastic nitinol, it has not been possible to find literature related to

CONTACT Joel C. R. Scott. Email: joel.scott@dal.ca, phone: 902-494-3052

computationally investigating the mechanisms responsible for radial force generation in 316L SS z-type self-expanding endovascular stent wires[3]. However, some resources are available which explore experimentally validated modeling of complex 316L SS self-expanding stent-graft assemblies[4, 5, 6].

Current numerical analyses of Abdominal Aortic Aneurysms (AAA) and EVAR focus on several topics. These include: stent-graft oversize, arterial remodeling due to the interaction of stent-grafts and artery walls[7, 8, 9, 10]; the prediction of aneurysm rupture based on sac pressure and wall stress/ strain[11, 12, 13, 14, 15, 16, 17, 18]; haemodynamics, drag, migration and endoleak[12, 19, 20, 21, 22, 23, 24]; bending and kinking[25, 26, 27]; as well as thrombus and calcification[24, 28, 29, 30].

Some existing analytical works make assumptions in regard to how force is generated in the stent. For example, Wang et al. examined a wire mesh stent as an equivalent thin-walled pressure vessel[31]; and Vad et al. used interference fitting theory for the contact pressure that develops at the interface of two concentric cylinders to experimentally validate their finite element model investigating the coefficient of friction for self-expanding stent-grafts[32]. Other examples would be the assumption made by Snowhill et al. that the mechanical reaction of a single stent bend could be extrapolated to get the radial force of a complete stent, or Fallone et al. assuming that Hooke's law could be used to determine radial force[33, 34, 35, 36]. This study aims to perform a more complete investigation into the mechanics of stent force generation, avoiding assumptions made in previous works. Results from this FEM study can be used in the development of an accurate analytical model.

2. Methods

2.1. Stents

Zenith z-type 316L stainless steel stents were used in this system (Figure 1). Material values are taken from the MatWeb material property database and are shown in Table 1[37]. The stent is modeled as an uncovered, geometrically accurate replica of a 12 mm (20.35 mm uncovered, fully expanded diameter) Zenith z-stent using one-dimensional beam elements.

A one-dimensional stent model is sufficient to model the bending behaviour of the long and thin stent wire to achieve the goal of this work to create a validated model to better understand the mechanisms responsible for radial force generation in a 316L SS self-expanding stent. Although using 3D elements to represent the stent may give a better through-thickness representation of strain, the increased computational requirement of this added complexity was not within reach of this study.

Table 1. Material properties of an annealed, cold drawn stainless steel 316L bar[37]

Property	Typical Value	Unit
Tensile strength, ultimate	585	MPa
Tensile strength, yield	380	MPa
Young's modulus	193	GPa
Density	0.008	g/mm^3
Poisson's ratio	0.3	

Figure 1. Single Zenith z-type stent wire

2.2. Experimental Procedures

Figure 2 shows a radial extensometer which was designed and sized specifically to measure the radial force exerted by endovascular stents at different levels of expansion.

The radial extensometer can be broken down into it's component parts as shown in Figure 3. The Mylar sheet, shown in red; the linear slide, load cell, and stent. Examining Figure 4 from '-x' to '+x', Mylar is threaded from a stationary anchor, around a primary roller, around the stent being tested, around a secondary roller, finally terminating at a moving anchor. The stent is constricted by displacing the moving Mylar anchor away from the stationary anchor at a rate of 0.329 mm/s, a value chosen to match that used by Clifton et al. who used a similar radial extensometer in their research[38]. The stent is constricted to 50 % of its original cross sectional area, then expanded by reversing the constriction procedure. The stent radius is measured both through an analytical method, converting linear slide motion to reduction in radius, as well as by using machine vision through a camera mounted on the side of the radial extensometer which looks down the center of the stent during constriction and expansion[39]. The radial force exerted by the stent on the Mylar film is read through a +x force gauge connected to the stationary anchor.

An investigation into the effect of changing the thickness of the Mylar film in the radial extensometer was published by Scott et al.[39]. The thickness of the Mylar film should not have an impact on the ability to validate this model as the thickness is

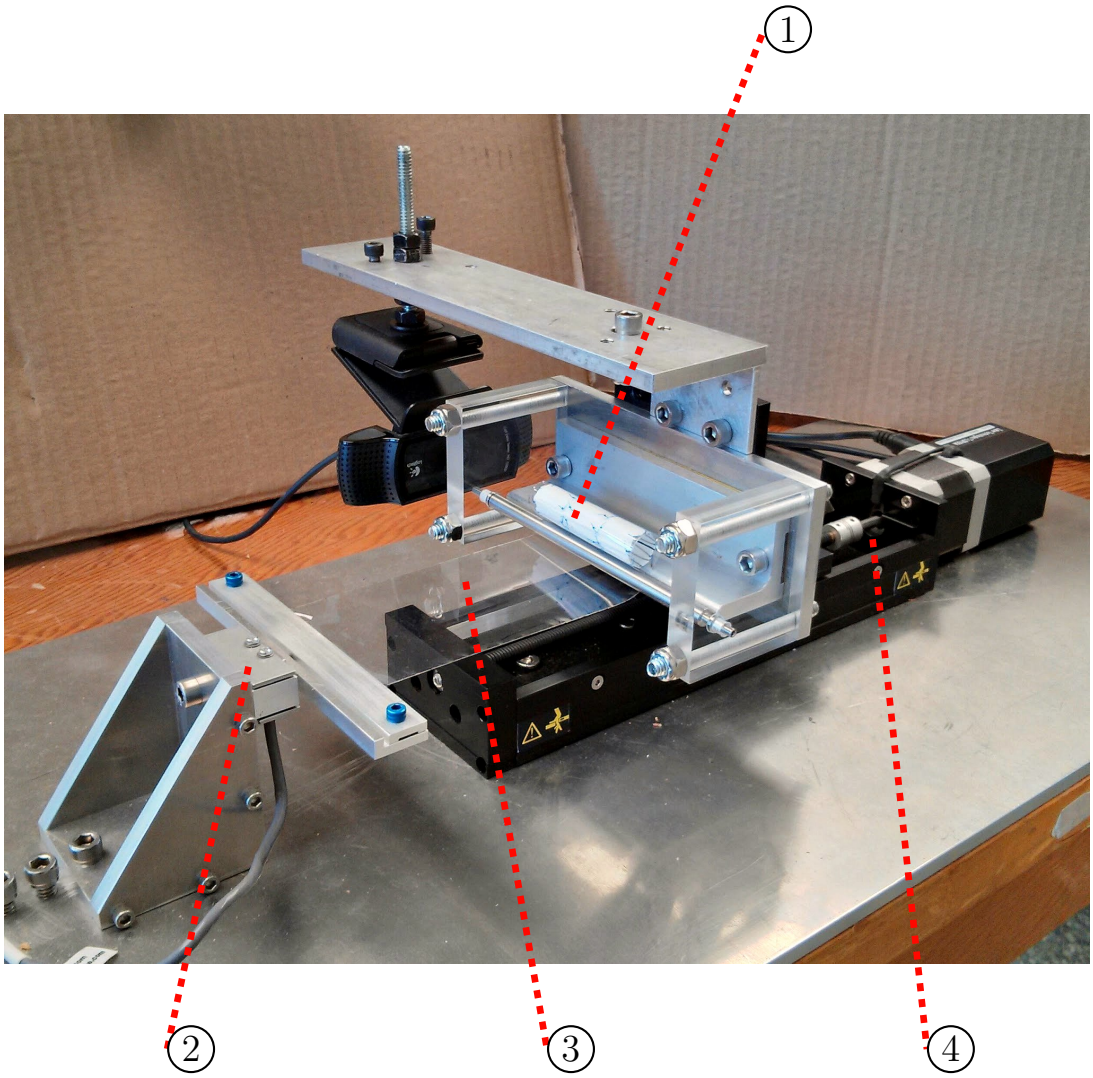

Figure 2. Extensometer system: 1–stent-graft, 2–force gauge, 3–Mylar film, 4–linear slide

kept constant between experiment and simulation.

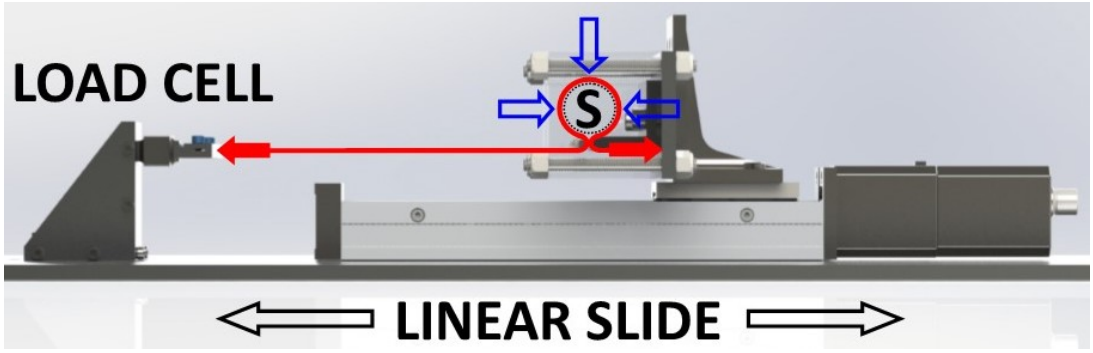

Figure 3. Generalized radial extensometer functionality

Using a novel, simplified, radial extensometer enabled the building and validation

of a simplified FE model in order to more closely analyze the mechanisms responsible for radial force generation in self expanding 316L SS stents. Commercially available options such as the MSI RX650 were both overly complex for designing into a FE model for the purposes of experimental validation, but also cost prohibitive to our group. Additionally, the experimental system and corresponding model were designed in part, to validate previous work by Clifton et al. who used a similar experimental setup[38].

2.3. FE Modeling

Five programs were used to create and analyze all finite element (FE) models in this work.

(1) **SolidWorks:** Used for computer aided design (CAD) of component geometries[40].
(2) **Hypermesh:** A FE pre-processor used for meshing solid geometries[41].
(3) **LS-DYNA:** A dynamic modeling program used to simulate changes in engineering properties throughout meshed geometries[42].
(4) **LS-PrePost:** A FE post-processor used for extracting meaningful data and visuals from completed simulations[43].
(5) **Python (x,y):** An interpreter for the Python language, as well as a software package catered toward the scientific community.

The model constructed as part of this study mimics the function of the novel radial extensometer used for experimental data collection, facilitating model validation. The final complex system was divided into five stages of development with each stage building upon the mesh, contact, and material model foundation validated by those before it. This step-by-step methodology ensures a reliable and accurate foundation for the complete system. All stages demonstrated effective material response, contact effectiveness and mesh convergence:

(1) Simple flat 2D Mylar specimen.
(2) 2D Mylar with 90° circular bend.
(3) 2D Mylar run around three rigid roller cylinders.
(4) 2D Mylar run around two rigid roller cylinders and a deformable stent analog cylinders.
(5) 2D Mylar run around two rigid roller cylinders and a deformable full stent geometry.

In the first foundational model, the flat 200 mm long by 60 mm wide section of Mylar was used to refine element formulation and material performance, as well as to determine whether deformation of the Mylar during stent testing would contribute error to experimental results. A converged model of a flat section of Mylar whose overall dimensions are the same as those in the final model was subjected to a 10 N force along a free end while the opposite end was fixed. Simulated results show the Mylar sheet reaching a peak stress of 16.91 MPa in the machine direction (+x to -x). This is 17.5 % of Mylar's yield stress of ∼96.5 MPa, consequently, plastic deformation is not likely, and the error due to elongation will be less than 2.7 %. As long as area reduction (AR) values are collected using the machine vision system using the webcam in Figure 2 of the radial extensometer, instead of through implicit calculation, AR error due to Mylar elongation is minimized. This is due to the fact that the AR calculation explicitly

estimates the radius of the deformed stent shape whilst other methods calculate the radius based on the amount of linear extension of the Mylar. All experimental tests performed for these studies use machine vision for AR calculation. Mylar elongation should not have a significant effect on experimental results because each test performed with the radial extensometer is forced to achieve 50 % AR.

In the complete simulation, the thin Mylar film was meshed using two-dimensional quadrilateral elements and modeled assuming a Hookean elastic material using LS-DYNA's "*MAT_ELASTIC" constitutive material model with material properties provided by DuPont Teijin Films (Table 2)[44]. This Mylar model was used in every subsequent simulation performed leading up to the final simulation.

Table 2. Material properties of Mylar provided by DuPont Teijin Films[44] (MD = machine direction, TD = transverse direction)

Property	Direction	Typical Value	Unit
Tensile strength, ultimate	MD	196	MPa
	TD	235	MPa
Young's modulus (tension)	MD	4805	MPa
	TD	5001	MPa
Young's modulus (compression)		$2726 - 2834$	MPa
Density		0.00139	g/mm^3
Poisson's ratio		0.38	

The rollers included in this simulation (Figure 4) are created as a stainless steel 316L rigid body and modeled using the "*MAT_RIGID" material model. The roller is modeled as a rigid body under the assumption that its deformation throughout testing is insignificant and has a negligible effect on model results. Using a rigid body material model will reduce simulation time by avoiding the calculation of unnecessary stress and strain results for the roller. All Mylar on roller contacts are modeled as frictionless two-dimensional quadrilateral elements throughout these works. This assumption creates a reasonable representation of the experimental setup, as the primary roller is bearing mounted. Additionally, the smooth aluminum surface of the secondary roller would only encounter friction if there were elastic deformation of the Mylar sheet, which was shown to be minimal. A mesh convergence study was undertaken which considered the effect of both Mylar and stent mesh size on peak force. A converged mesh size of 0.25 mm and 0.4 mm was determined for the Mylar and stent respectively. A thorough description of the FE model and mesh convergence study is given in Appendix A.

For the Mylar to roller contact definition, a penalty-based contact algorithm was employed using LS-DYNA's "*CONTACT_AUTOMATIC_SURFACE_TO_SURFACE" contact interface definition. In a penalty-based contact, penetration of contacting surfaces is eliminated by applying a force proportional to the penetration depth of any infiltrating surfaces[45]. This is in contrast to constraint-based contacts where two contiguous surfaces are bound together, sharing nodes and avoiding penetration or separation. This surface-to-surface card was selected over others due to the types of elements coming into contact: the Mylar shell surface and the rigid roller shell surface. An automatic contact was selected because it is less dependent on reliable contact orientation, thereby improving contact stability[45, 46]. For a rigid body in any penalty-based contact, LS-DYNA advises that contact surface node spacing of a rigid body be no coarser than the mesh of deformable parts which it comes into contact with

in order to ensure proper distribution of contact forces. Because no stress or strain calculations are performed for a rigid body, refining the mesh of a rigid body has little effect on CPU requirements[45]. For these reasons, the rigid roller was modeled with the same mesh density as the Mylar sheet.

The roller furthest in the '-x' direction was made free to rotate. As the Mylar mesh slides over the roller mesh during simulation; x, y and z penalty forces ensure no contact penetration occurs. Even though contact between Mylar and rollers is frictionless, tangential contact penalty forces were growing so large prior to the Mylar sliding over the roller that the contact was failing. Allowing the frictionless roller to rotate eliminated both this buildup of contact penalty force and unintentional contact penetration.

The geometrically correct stent model was modeled using 1-D beam elements and uses the same 316L stainless steel elastic material model as the rollers whose properties are defined in Table 1. Due to the symmetry of the experimental system and of stent loading/unloading, the stent stays centered in the experimental apparatus throughout testing, and is therefore not affixed axially in the experimental setup. The stent is also purposefully not constrained axially so as to avoid interfering in any way with radial force data collection. In the FE model however, the stent is constrained in the axial direction using a single symmetrical node at the peak of each bend on one side of the stent. Only one side of the stent was constrained to ensure the stent could still extend in the z-direction during constriction. The stent is constrained in the FE model to aid model convergence especially during low friction analysis.

Stent self-contact is included using "*CONTACT_AUTOMATIC_GENERAL" to ensure that during constriction, the stent can't pass through itself. If beam elements from different sections of the stent come close enough to touch each other during constriction, the ability for the stent to interact with itself is crucial to model accuracy.

Contact definition variables for slave and master penalty stiffness scaling factors as well as sliding interface penalty scaling factors were manipulated to achieve a stable contact between the significantly varying thicknesses and Young's moduli of Mylar and stainless steel. These values ensure that contact penetration does not occur throughout the simulation while using a penalty based contact algorithm. The slave scaling factor (SFS) and master scaling factor (SFM) were both found to be most effective with a value of 5.0 for contact between Mylar and rollers. For the stent-Mylar contact, SFS and SFM were set to 0.0 and 10.0 respectively. The contact between stent and Mylar was defined using the "*CONTACT_NODES_TO_SURFACE" contact definition. Mylar shell elements only need to check for contact penetration on one side throughout simulation and the direction of surface orientation is known, therefore, the Mylar to stent contact may use a non-automatic formulation to reduce simulation time[47]. This contact type is also effective for a beam to shell surface contact like that between the stent and Mylar[48]. This one-way contact checks each slave node (stent beam elements) for penetration through the master surface (Mylar shell elements)[45].

Simulated force data was collected by mimicking the functionality of the radial extensometer experimental setup. To achieve this, all nodes on the most '-x' edge of the Mylar in Figure 4 were constrained using '*BOUNDARY_SPC_SET_ID' to ensure the nodes were only free to move in the 'x' direction. This represents the section of Mylar clamped in the force gauge fixture (Item 2 in Figure 2). Both rollers, and all nodes on the most '+x' edge of the Mylar in Figure 4, were assigned a prescribed motion boundary condition using '*BOUNDARY_PRESCRIBED_MOTION_NODE_ID' and '*BOUNDARY_PRESCRIBED_MOTION_SET_ID' respectively. The model was configured to ensure the same rate of constriction as in the experimental setup by sep-

arating the two Mylar anchors at a velocity of 0.329 mm sec. The "nodfor" database file was output during simulation, which allows forces registered by constrained nodes, and nodes with prescribed motion to be output and plot. Force data for all nodes on the most '-x' edge of the Mylar in Figure 4 were output throughout the simulation to tune the model in comparison to experimental results using Coulomb friction constants. The static and dynamic coefficients of friction are both set equal to each other at 0.0025, eliminating dependence of the results on the relative velocity of the surfaces in contact. This constant not only serves to introduce frictional effects into the simulation but also as a method of accounting for unknown sources of error during model fitting.

A non-linear implicit solver was used primarily to lengthen simulated duration to real world values without the enormous increase in simulation run time that would be associated with the explicit solver. Increasing the time step to reduce the run time for an explicit solver would require mass scaling. Scaling the mass of small components present in the final model would have a significant impact on collected force results ($F = ma$), while also increasing inertia and momentum. The final FE model is considered non-linear because it simulates contacting parts and experiences a large amount of deformation. Figure 4 shows a rendering of the final completed simulation.

A comparison of fully expanded and fully constricted simulation states is shown in Figure 5.

3. Results

3.1. Model Fit

As previously stated, because this model was designed to match the experimental setup of the radial extensometer, it is possible to fit the final converged simulation to experimental results. All presented experimental results are the average of three separate data sets collected in three distinct trials using the radial extensometer. Further explanation of the radial extensometer and data collection methodology has been published separately by Scott et al.[39].

Modeled and experimental data sets compare an uncovered 12 mm (uncovered diameter = 20.35 mm) stent being constricted to a diameter equal to that of a covered stent constricted to 50 % AR (final diameter = 8.49 mm). Because these data sets represent the same motion and mechanics, lining up known values for the center point (the point of peak constriction) of modeled and experimental data will give an accurate comparison of the two results.

The Coulomb friction constant is used as a fitting parameter to match modeled and experimental data as closely as possible. Static and dynamic Coulomb constant values are kept equal throughout model fitting. The Coulomb friction coefficient should remain the same regardless of the dimensions of the 316L SS stent being modeled, so long as material parameters in the simulation remain the same. All experiments carried out with the radial extensometer and simulated using this model use the same 316L SS on Mylar contact. Investigating different materials would require resetting the friction coefficient. Employing this simplification of using the Coulomb constant as a tuning parameter allows for a first pass on stent design prior to defining all of the significantly more complex friction mechanisms such as stiction and shearing, which are not modeled and are captured by the fitting parameter

In general, as the Coulomb constant grows, peak force will increase and force mea-

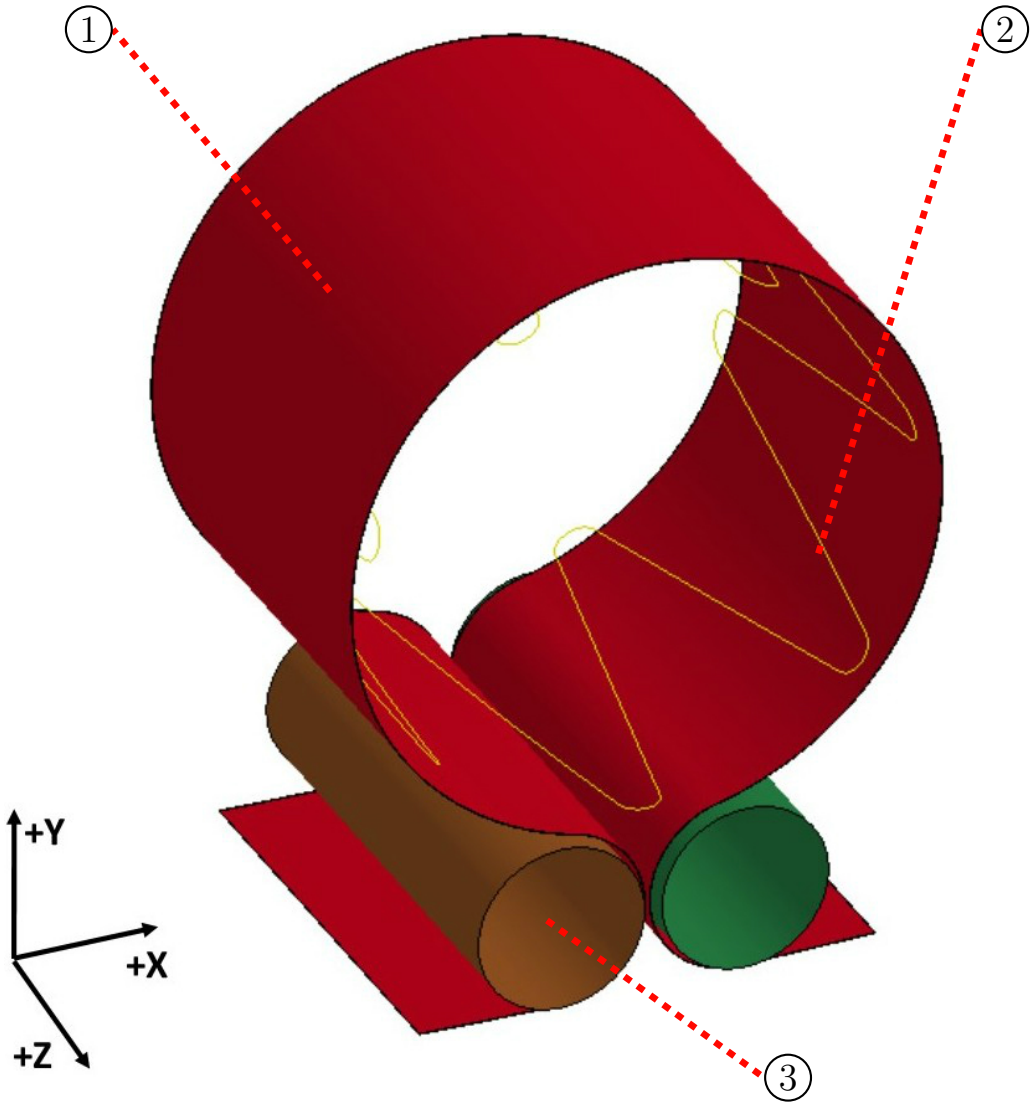

Figure 4. Final completed model: 1 - Mylar with friction, 2 - free stent, 3 - rigid rollers

sured during expansion will decrease. As seen in Figure 6, a frictionless model may best match linear experimental results encountered following the initial force drop-off at the onset of expansion, however, to best match the entire force profile observed during stent expansion, a contact formulation including friction was used.

With a completed convergence study, the Coulomb constant can be optimized to yield a better comparison between modeled and simulated results. Observation of the frictionless curve in Figure 6 reveals that friction is not solely responsible for force profile non-symmetry, the radial extensometer and stent mechanics may have a larger impact on collected force data than previously thought. Figure 6 demonstrates that friction has a large impact on the smoothness and linearity of the radial force profile during expansion.

Model fit success was determined using the coefficient of determination (r^2), standard error of the estimate (SE), and mean percent error (MPE) values calculated using Equations 1−3. As can be seen in Table 3, a Coulomb friction constant of 0.0025 best matches experimental data considering multiple error measures: an r^2 value of 0.946,

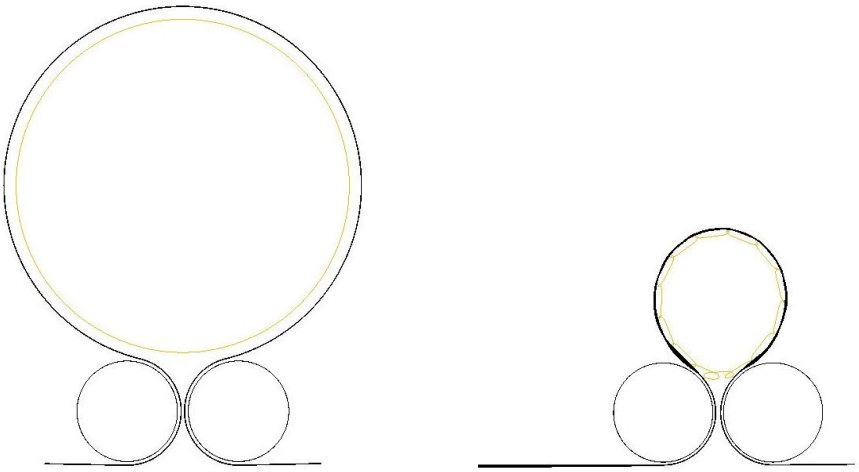

(a) Simulation start (original) **(b)** Fully constricted

Figure 5. Completed simulation constriction with rigid rollers; free stent and Mylar with friction

a standard error of 0.099 N, and a MPE of 1.69 %. These results show good fit between experimental and modeled results.

A Coulomb friction constant of 0.0025 falls within the range used by Vad et al.[32], however, it is important to note they did not test stents as small as 12 mm in diameter. Also, the stents they tested were of a different wire configuration. All tests used 4 CPU (central processing unit) cores and 500 million words of memory.

$$r^2 = 1 - \frac{\sum_{t=1}^{n} \left(Y_{1,t} - Y_{2,t}\right)^2}{\sum_{t=1}^{n} \left(Y_{1,t} - \bar{Y_1}\right)^2} \tag{1}$$

$$SE = \sqrt{\frac{\sum_{t=1}^{n} \left(Y_{1,t} - Y_{2,t}\right)^2}{n}} \tag{2}$$

$$MPE = \frac{100}{n} \sum_{t=1}^{n} \frac{Y_{1,t} - Y_{2,t}}{Y_{1,t}} \tag{3}$$

where r^2 = coefficient of determination, $SE_{Estimate}$ = standard error of the estimate (N), Y_1 = original force dataset (N), $\bar{Y_1}$ = mean of force dataset (N), Y_2 = model fit force dataset (N), n = number of values in dataset.

Referencing Table 3, it is interesting to note that as friction rises above a Coulomb constant of 0.05, there is a rapid decline in coefficient of determination, peak simulated force and simulation run-time, while standard error rises significantly. Coulomb constant values above 0.05 are also detrimental to simulation performance and should not be used.

The final converged model, fit to experimental data with a coulomb constant of 0.0025 is presented in Figure 7. Modeled data is offset by 12.351 s to line up the point at which modeled and experimental data both reach a constriction of 50 %AR. Results for the period of stent expansion only are shown in Figure 8. Results are plotted with time as the dependant variable, instead of stent radius, to minimize error included in

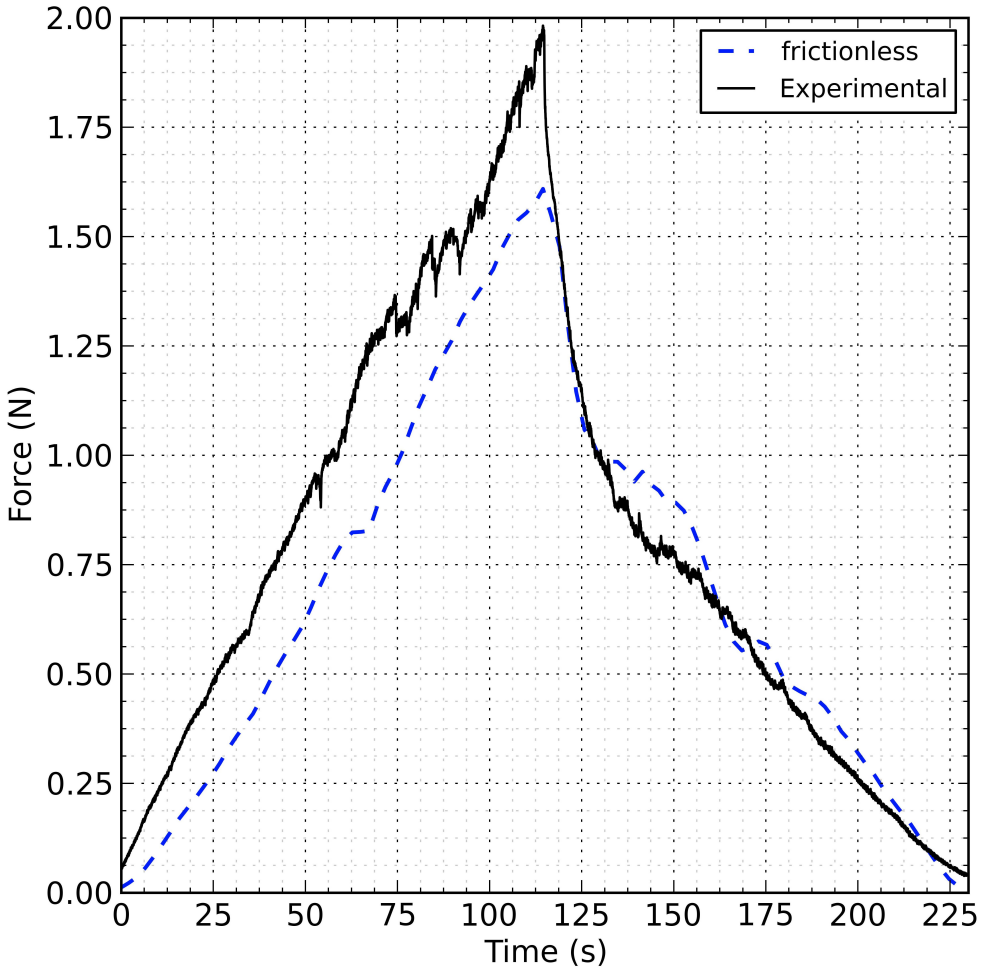

Figure 6. A comparison of experimental results and simulated results without model fitting (Coulomb friction)

the comparison of simulated and experimental results during model validation. Future research could certainly plot radial force vs. stent radius with a disclaimer that error due to radius being calculated and observed using machine vision, instead of being physically measured, is contained in the results

4. Discussion

A complete, converged, and experimentally validated model enables future research to investigate not only the mechanical properties of self-expanding z-stents, but also the mechanisms responsible for radial force generation. The presented method of being able to calibrate and validate modeled results using the radial extensometer provides advantages over non-experimentally validated methods through improvements in modeled accuracy. Collecting stent radius and percent area reduction data using machine vision also enables the simulation and experimental validation of non-circular deformations of the stent. Model analysis should also prove useful in understanding what impact the radial extensometer may have on collected data.

The interaction between stent and Mylar can be visualized in the full system rep-

Table 3. Model fitting results

Coulomb	CPU Time (s)	F_{Peak} (N)	r^2	SE (N)	MPE (%)
0.0	98638	1.61	0.967	0.072	−8.29
0.00001	92002	1.97	0.852	0.150	12.38
0.0001	91927	2.14	0.842	0.155	11.10
0.0005	93533	2.04	0.860	0.146	11.61
0.001	96466	2.10	0.914	0.114	3.76
0.0025	**98638**	**2.04**	**0.946**	**0.099**	**1.69**
0.005	93534	2.12	0.843	0.154	11.21
0.0075	95597	2.04	0.865	0.143	11.73
0.01	93155	2.15	0.811	0.169	11.28
0.02	97391	2.13	0.934	0.100	4.55
0.05	99542	2.11	0.919	0.111	11.52
0.075	81722	2.40	0.776	0.184	11.53
0.1	81794	2.47	0.750	0.195	13.42
0.2	81794	2.62	0.502	0.275	26.70

resentation of von Mises stress in Figure 9. Interestingly, contact and force transfer between the stent and Mylar sheet during expansion seems to be limited to the legs and not the bends of the stent as shown by areas of peak von Mises stress in this figure. No plastic deformation was observed experimentally, nor was it modeled or investigated as part of this research. Elastic models were used for the stent and Mylar.

An analysis was performed to determine whether reaction forces experienced at both Mylar anchors were equal. Using the system presented in Figure 4, the free-body diagram (FBD) in Figure 10 shows that T_1 and T_2 should display an equal result unless interfered with by friction. Figure 11 compares T_1 and T_2 and reveals the difference between them, labeled $F_{Unknown}$, which most likely represents frictional effects. The magnitude of $F_{Unknown}$ changes direction following the switch from constriction to expansion, as would be expected for friction.

A comparison of modeled and experimental data, without any model fitting, still reveals satisfying results. In Figure 6, model and experiment match closely for the expansion of the stent, but not for compression and peak force. Given that expansion is clinically important, this is a very positive outcome. However, static friction was selected as a fitting parameter in order to more closely match experimental results. The close agreement between the model and experiment in Figure 11 demonstrates that it is reasonable to assume that the discrepancy between modeled and experimental results in Figure 6 are caused by friction. The value of $F_{Unknown}$ is logically assumed to be the reason behind major under-prediction of radial forces during constriction, while minor over-prediction during expansion is attributed to the damping of expansion and radial force values. Another possible contributor to the observed discrepancy is the known variation of elastic modulus within the 316 stainless steel family of alloys (e.g. medical grade 316LVM) given the limited specific knowledge of the alloy composition of the stent wire used in this study.

With or without model fitting (friction), the radial force during expansion and contraction is non-symmetric, meaning there must be certain stent or extensometer mechanical properties which are still not well understood. Continuing to improve our understanding of the mechanical properties of stents through the entire cycle of expansion and contraction will likely yield meaningful results, however, there is a specific

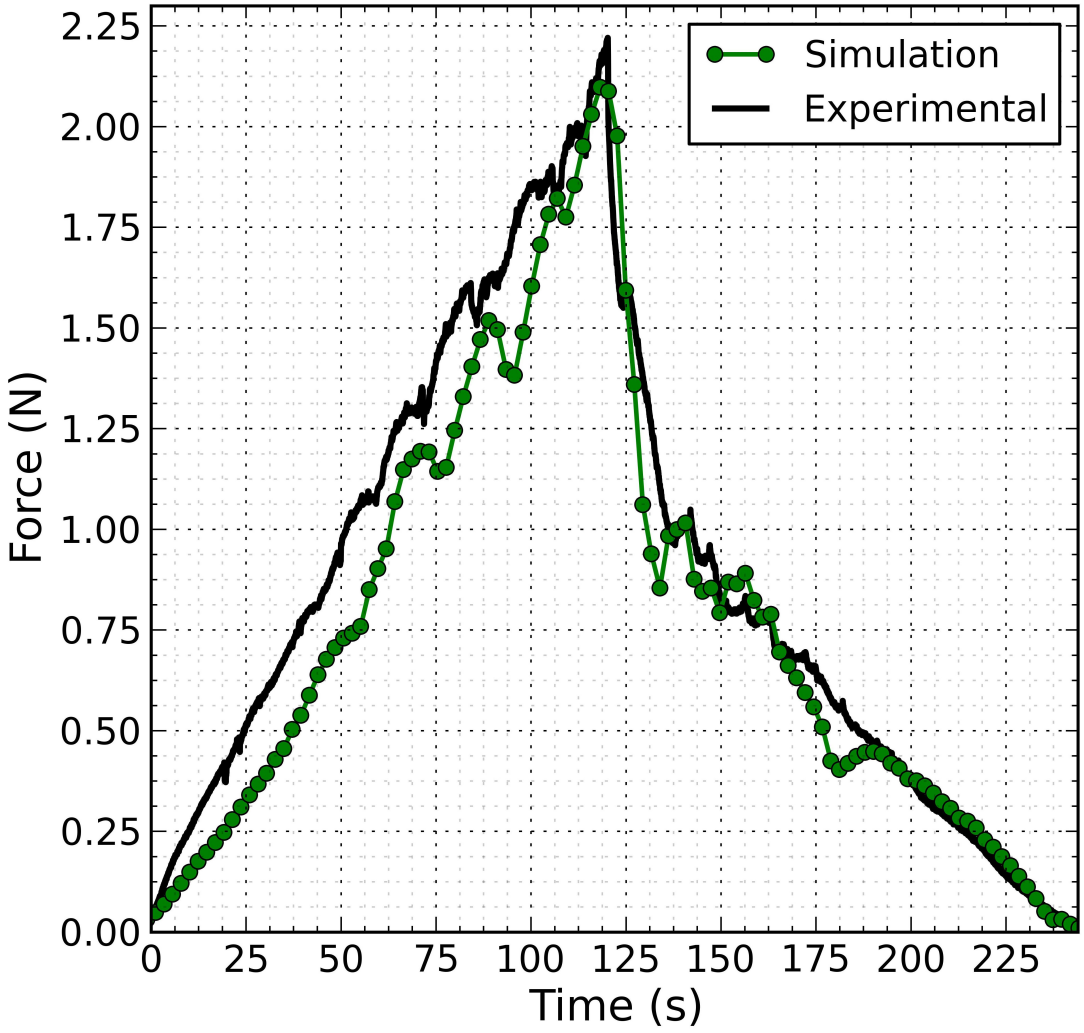

Figure 7. Completed model fit and comparison of full simulated and experimental data profile

region of data which contributes significantly more to the performance of current stents in-vivo which should be focused on. The more linearly decreasing section of Figure 8 ($\sim$145 s onward) is the area we're interested in from a clinical perspective. It represents a $10-20\,\%$ oversize of the stent compared to the original outer arterial diameter which is commonly used to size z-type endovascular stents [24, 49]. In this more linear region there is a randomness in both the experimental and the modeled data, however, the errors are within a similar range of eachother, and appear at times to be somewhat inversely proportional. From $\sim$195 s on we have consistently smooth and linear data.

Unrolling the FBD of Figure 10, a new FBD perspective (Figure 12) can be visualized to help understand $F_{Unknown}$ from Figure 11. Assuming uniformly distributed loads, equal roller contact area, and frictionless rollers, a value of $F_{Unknown}$ during constriction can be defined in a closed form model using the analysis performed from Equation 4 to 11.

Assuming static friction,

$$F_{\mu s} = \mu_s F_R \tag{4}$$

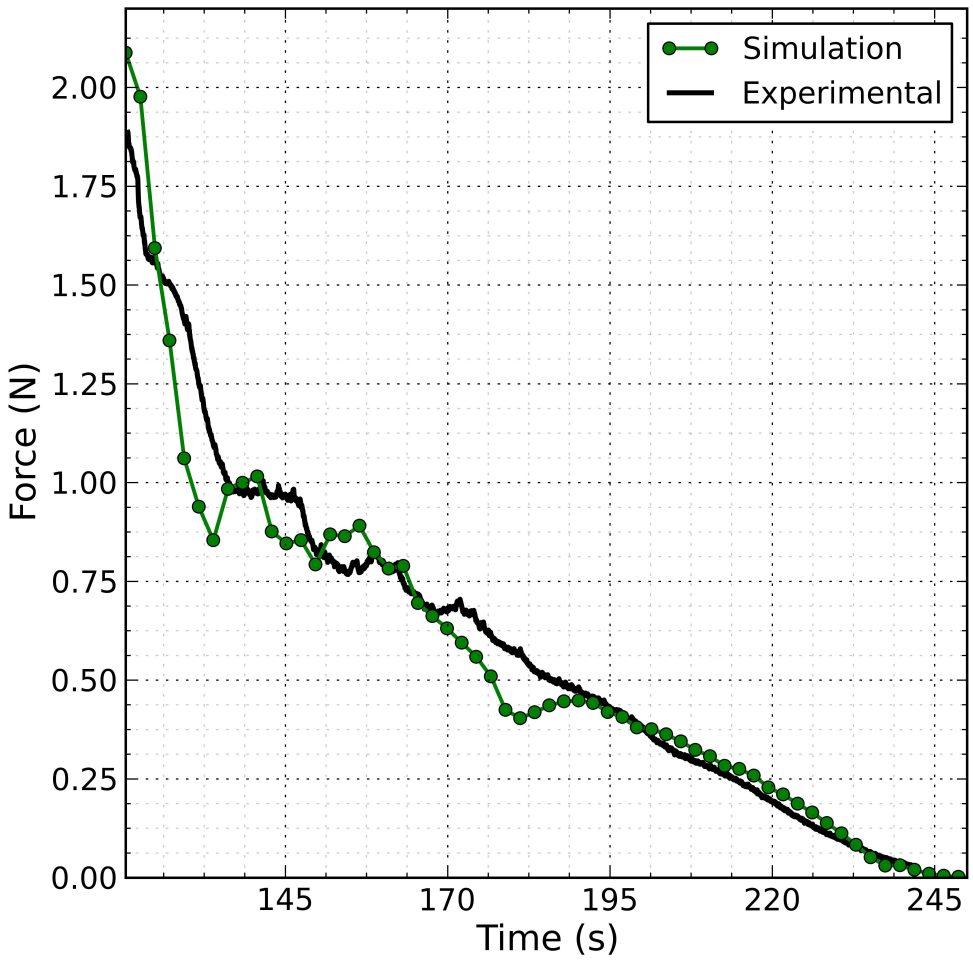

Figure 8. Completed model fit and comparison of simulated and experimental data during expansion only

where $F_{\mu s}$ = static friction force (N), μ_s = static Coulomb friction constant, F_R = radial force (N). Equilibrium equations become,

$$\sum F_x = 0 \tag{5}$$

$$T_1 = T_2 + F_{\mu s} \tag{6}$$

$$\sum F_y = 0 \tag{7}$$

$$F_R = N_1 + N_2 \tag{8}$$

where F_x/F_y = x and y-component forces (N), T_1/T_2 = Mylar tensile forces (N), N_1/N_2 = normal roller forces (N). Assuming a linear radial stiffness,

$$F_R = kAR \tag{9}$$

where k = radial stiffness (N/mm^2), AR = area reduction (%). Substituting Equation 4 into 6,

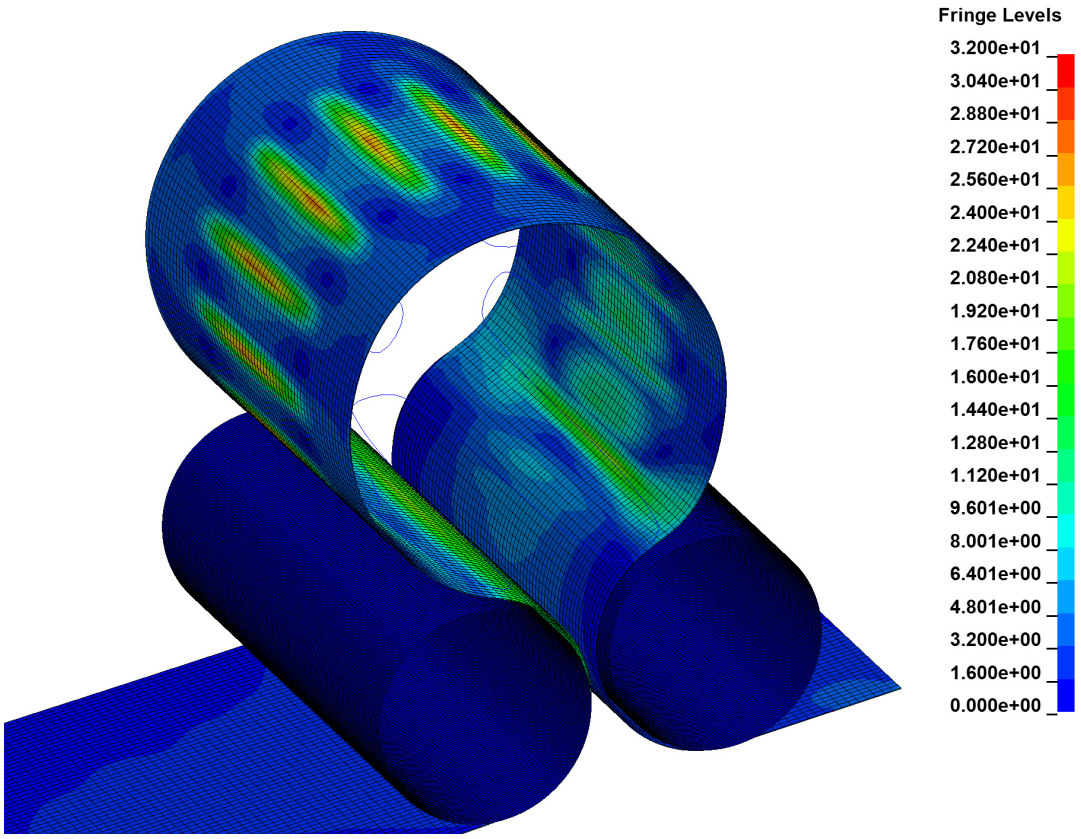

Figure 9. von Mises stress (MPa), full model at 157.5 s

$$T_1 = T_2 + \mu_s F_R \tag{10}$$

Finally, substituting Equation 9 into 10,

$$T_1 = T_2 + \mu_s kAR \tag{11}$$

Solving for the $F_{Unknown}$ force profile from figure 11, Equation 11 becomes:

$$F_{Unknown} = T_1 - T_2 = \mu_s kAR \tag{12}$$

5. Conclusions

A converged FE model of a radial extensometer testing a 12 mm stent was developed to analyze stent mechanics and provide a tool for future stent development. Validation of the converged radial force profile during expansion provided a good fit, attaining an r^2 of 0.946, a standard error of 0.099 N, and a MPE of 1.69 % when compared to experimental results.

Analysis of the completed FE model provides evidence that the non-symmetric force profile created through comparison of results during constriction and expansion (e.g.

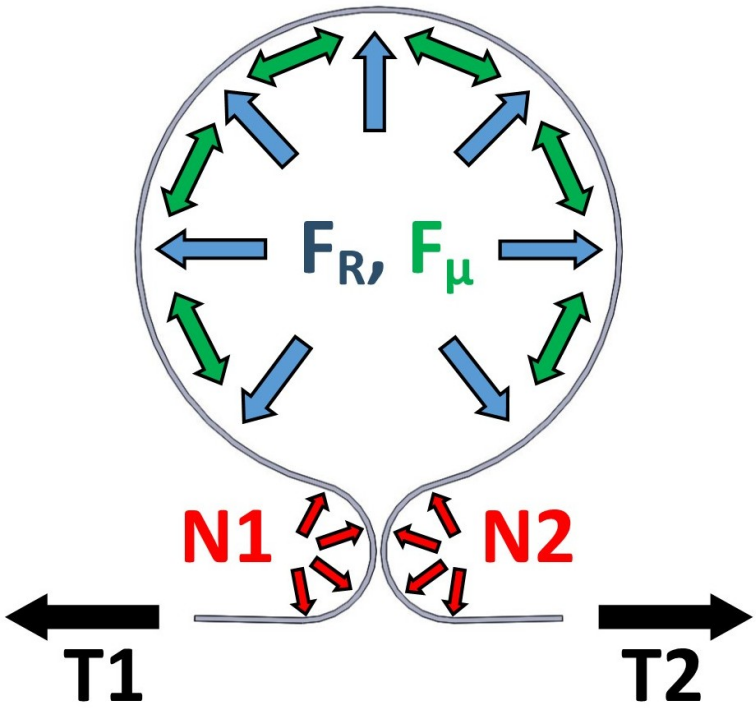

Figure 10. Free-body diagram of contributing reactions. F_R = radial force, F_μ = friction force (constriction and expansion), N_1/N_2 = normal roller forces, T_1/T_2 = Mylar tensile forces

Figure 7) is not solely due to frictional effects. Simulation results show that both the interaction between the stent and radial extensometer rollers, as well as stent mechanics, have an impact on radial force generation.

These new tools could be used to collect data required to shift from an inexact stent selection methodology based on a generalized range of prosthetic oversize, to one where stents are developed to generate an ideal radial force for each patient's specific characteristics. Additionally, this validated model and its subsequent improved generations could be used to calculate data ingested by patient specific stent design tools such as that designed by Scott et al.[50].

Now that the FE model is converged and validated using experimental data, the model could be used to analyze 316L SS stents of differing diameters, leg lengths. bend radii, wire diameter, and bend angle. However, the model would have to be re-validated if any new components or materials were introduced, or if the experimental design was altered in any way.

There are several other pathologies treated with EVAR that would benefit from the ability to measure and manipulate the radial force generated by their associated prosthetics. Devices used in more delicate circumstances such as vena cava stenosis and aortic dissection, where it is important to minimize the amount of stress imparted on the weak or weakened vessel, would benefit disproportionately from this ability[51, 52, 53, 54].

In future stent wire simulations, along with varying material properties, alterations to wire cross section geometry could be used to manipulate torsion, s-bending and t-bending moments. Future work should attempt to determine the contributions of torsion, s-bending, and t-bending moments on the radial force produced by stent wires.

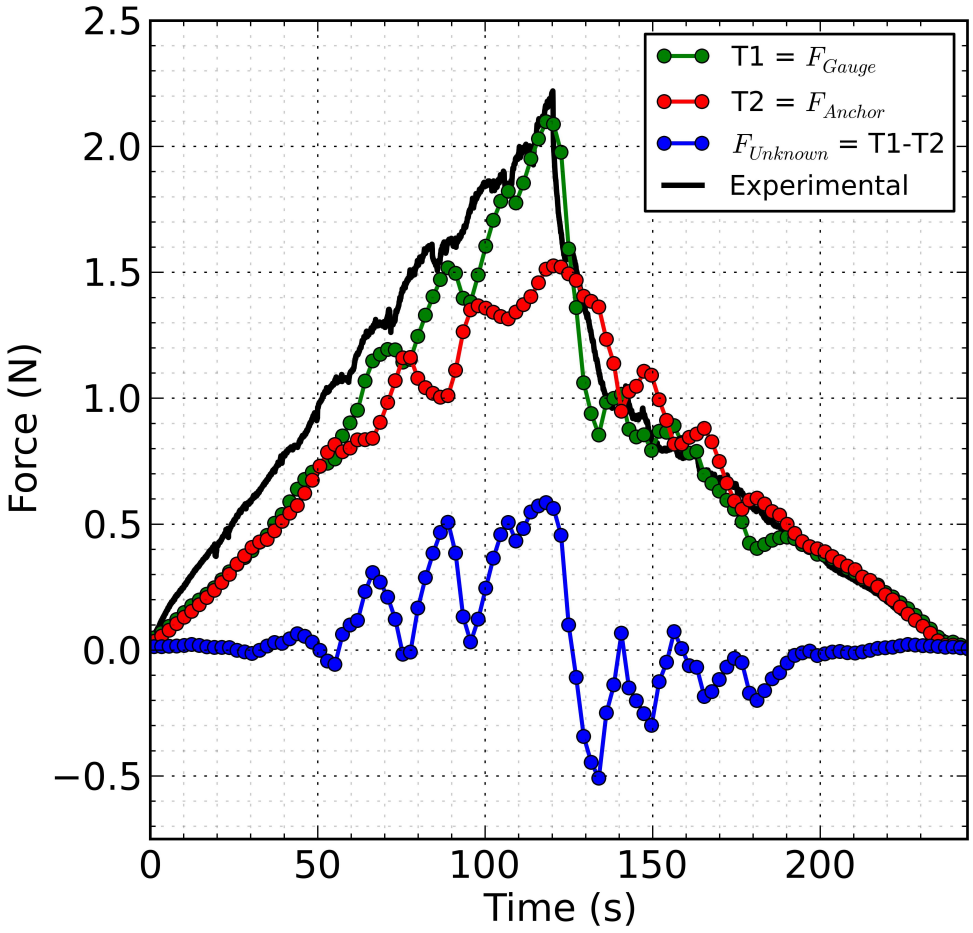

Figure 11. Comparison between force gauge and linear force data from the moving anchor

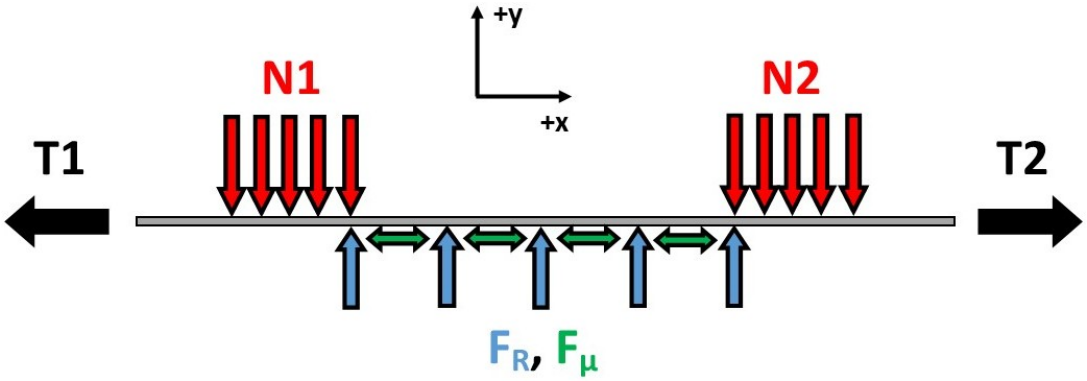

Figure 12. Unrolled free body diagram of contributing reactions. F_R = radial force, F_μ = friction force (constriction and expansion), N_1/N_2 = normal roller forces, T_1/T_2 = Mylar tensile forces

Developing the ability to predictably control these mechanical stent characteristics could significantly improve the precision of future stent designs.

Future work should also analyze the method of conversion from stent radial force to the linear force measured by the experimental force gauge and how these two compare. An accurate representation of radial force is very important to understanding friction

between the artery wall and stent, as well as for determining what radial force is needed for solid stent fixation. Future expansions of this preliminary simulation could both investigate the impact of varying haemodynamic drag loads on stent fixation, as well as the likelihood of endoleak at different levels of oversize and AR.

Adoption of the validated FE model and radial extensometer by others could help establish a cost effective, consistent platform for both the comparison of results, as well as crowd sourced cataloging of the performance of existing prosthetics.

Acknowledgments

This work has been supported by a grant from the Natural Sciences and Engineering Research Council of Canada.

Conflict of Interest

The authors declare no potential conflicts of interest.

References

[1] *316L Stainless Steel*. MatWeb, LLC. URL: http://matweb.com/search/DataSheet.aspx?MatGUID=c02b8c0ae42e459a872553e0ebfab648 (visited on 11/22/2020).

[2] Dorothy B. Abel et al. "Evolution and Future of Preclinical Testing for Endovascular Grafts". In: *Journal of Endovascular Therapy* 13.5 (2006), pp. 649–659. DOI: 10.1583/06-1872.1. eprint: http://jet.sagepub.com/content/13/5/649.full.pdf+html.

[3] Anne Amblard et al. "Analysis of type I endoleaks in a stented abdominal aortic aneurysm". In: *Medical Engineering & Physics* 31.1 (2009), pp. 27–33. DOI: http://dx.doi.org/10.1016/j.medengphy.2008.03.005.

[4] S. De Bock et al. "Filling the void: A coalescent numerical and experimental technique to determine aortic stent graft mechanics". In: *Journal of Biomechanics* 46.14 (2013), pp. 2477–2482. DOI: http://dx.doi.org/10.1016/j.jbiomech.2013.07.010.

[5] Alessandro Borghi et al. "Effect of Stent Radial Force on Stress Pattern After Deployment: A Finite Element Study". In: *Journal of Materials Engineering and Performance* 23.7 (2014), pp. 2599–2605. DOI: 10.1007/s11665-014-0913-z.

[6] *Contact modeling in LS-DYNA*. Livermore Software Technology Corporation. URL: http://www.dynasupport.com/tutorial/ls-dyna-users-guide/contact-modeling-in-ls-dyna (visited on 02/13/2015).

[7] *Contact Overview*. Livermore Software Technology Corporation. URL: http://www.dynasupport.com/howtos/contact/contact-overview (visited on 02/13/2015).

[8] Michele Conti. "Finite element analysis of self-expanding braided wirestent". Belgium: Ghent University, 2007.

[9] Nicolas Demanget et al. "Computational comparison of the bending behavior of aortic stent-grafts". In: *Journal of the Mechanical Behavior of Biomedical Materials* 5.1 (2012), pp. 272–282. DOI: 10.1016/j.jmbbm.2011.09.006.

[10] Nicolas Demanget et al. “Severe Bending of Two Aortic Stent-Grafts: An Experimental and Numerical Mechanical Analysis”. English. In: *Annals of Biomedical Engineering* 40.12 (2012), pp. 2674–2686. DOI: 10.1007/s10439-012-0618-0.

[11] Nicolas Demanget et al. “Finite Element Analysis of the Mechanical Performances of 8 Marketed Aortic Stent-Grafts”. In: *Journal of endovascular therapy : an official journal of the International Society of Endovascular Specialists* 20 (Aug. 2013), pp. 523–35. DOI: 10.1583/12-4063.1.

[12] Nicolas Demanget et al. “Finite element analysis of the mechanical performances of 8 marketed aortic stent-grafts”. In: *Journal of Endovascular Therapy* 20.4 (2013), pp. 523–535.

[13] S. Dendo et al. “Severe obstruction of the superior vena cava caused by tumor invasion recanalization using a PTFE-covered Z stent”. English. In: *Journal of Cardiovascular Surgery* 43.2 (Apr. 2002), pp. 287–90.

[14] Barry J. Doyle, John Killion, and Anthony Callanan. “Use of the photoelastic method and finite element analysis in the assessment of wall strain in abdominal aortic aneurysm models”. In: *Journal of Biomechanics* 45.10 (2012), pp. 1759–1768. DOI: http://dx.doi.org/10.1016/j.jbiomech.2012.05.004.

[15] Barry J. Doyle et al. “Identification of rupture locations in patient-specific abdominal aortic aneurysms using experimental and computational techniques”. In: *Journal of Biomechanics* 43.7 (2010), pp. 1408–1416. DOI: http://dx.doi.org/10.1016/j.jbiomech.2009.09.057.

[16] B. Fallone, S. Wallace, and C. Gianturco. “Elastic Characteristics of the Self-expanding Metallic Stents”. In: *Investigative Radiology* 23 (5 1988), pp. 370–376.

[17] C Alberto Figueroa et al. “A Computational Framework for Fluid-Solid-Growth Modeling in Cardiovascular Simulations”. In: *Computer methods in applied mechanics and engineering* 198 (45-46 Sept. 2009), pp. 3583–3602.

[18] Mark Fillinger. “The Long-Term Relationship of Wall Stress to the Natural History of Abdominal Aortic Aneurysms (Finite Element Analysis and Other Methods)”. In: *Annals of the New York Academy of Sciences* 1085.1 (2006), pp. 22–28. DOI: 10.1196/annals.1383.037.

[19] *HyperMesh*. Altair. URL: www.altairhyperworks.com/Product,7,HyperMesh.aspx (visited on 11/19/2014).

[20] Ryan Jean-Baptiste, DavidM. Williams, and JosephJ. Gemmete. “Successful Treatment of Superior Vena Cava Rupture with Placement of a Covered Stent: A Report of Two Cases”. English. In: *CardioVascular and Interventional Radiology* 34.3 (2011), pp. 667–671. DOI: 10.1007/s00270-011-0128-8.

[21] CliftonR. Johnston et al. “The Mechanical Properties of Endovascular Stents: An In Vitro Assessment”. English. In: *Cardiovascular Engineering* 10 (3 2010), pp. 128–135. DOI: 10.1007/s10558-010-9097-9.

[22] C. Kleinstreuer et al. “Computational mechanics of Nitinol stent grafts”. In: *Journal of Biomechanics* 41.11 (2008), pp. 2370–2378. DOI: 10.1016/j.jbiomech.2008.05.032.

[23] Ethan O. Kung et al. “In Vitro Validation of Finite-Element Model of AAA Hemodynamics Incorporating Realistic Outlet Boundary Conditions”. In: *Journal of Biomechanical Engineering* 133 (4 Feb. 2011), p. 041003.

[24] Zhonghua Li and Clement Kleinstreuer. “Blood flow and structure interactions in a stented abdominal aortic aneurysm model”. In: *Medical Engineering and Physics* 27.5 (2005), pp. 369–382. DOI: http://dx.doi.org/10.1016/j.medengphy.2004.12.003.

[25] *LS-DYNA*. Livermore Software Technology Corporation. URL: www.lstc.com/products/ls-dyna (visited on 11/19/2014).

[26] *LS-PrePost*. Livermore Software Technology Corporation. URL: www.lstc.com/products/ls-prepost (visited on 11/19/2014).

[27] Francesco Migliavacca et al. "Stainless and shape memory alloy coronary stents: a computational study on the interaction with the vascular wall". English. In: *Biomechanics and Modeling in Mechanobiology* 2.4 (2004), pp. 205–217. DOI: 10.1007/s10237-004-0039-6.

[28] I.V. Mohan, R.J.F. Laheij, and P.L. Harris. "Risk Factors for Endoleak and the Evidence for Stent-graft Oversizing in Patients Undergoing Endovascular Aneurysm Repair". In: *European Journal of Vascular and Endovascular Surgery* 21.4 (2001), pp. 344–349. DOI: http://dx.doi.org/10.1053/ejvs.2000.1341.

[29] D.S. Molony et al. "A Computational Study of the Magnitude and Direction of Migration Forces in Patient-specific Abdominal Aortic Aneurysm Stent-Grafts". In: *European Journal of Vascular and Endovascular Surgery* 40.3 (2010), pp. 332–339. DOI: http://dx.doi.org/10.1016/j.ejvs.2010.06.001.

[30] David S Molony et al. "Fluid-structure interaction of a patient-specific abdominal aortic aneurysm treated with an endovascular stent-graft". In: *Biomed Eng Online* 8 (2009), p. 24.

[31] David S. Molony et al. "Geometrical Enhancements for Abdominal Aortic Stent-Grafts". In: *Journal of Endovascular Therapy* 15.5 (2008), pp. 518–529. DOI: 10.1583/08-2388.1. eprint: http://jet.sagepub.com/content/15/5/518.full.pdf+html.

[32] L. Morris et al. "A mathematical model to predict the in vivo pulsatile drag forces acting on bifurcated stent grafts used in endovascular treatment of abdominal aortic aneurysms (AAA)". In: *Journal of Biomechanics* 37.7 (2004), pp. 1087–1095. DOI: http://dx.doi.org/10.1016/j.jbiomech.2003.11.014.

[33] *Mylar Physical-Thermal Properties*. DuPont Teijin Films. URL: http://usa.dupontteijinfilms.com/informationcenter/downloads/Physical_And_Thermal_Properties.pdf (visited on 01/20/2014).

[34] F. Nematzadeh and S.K. Sadrnezhaad. "Effects of Crimping on Mechanical Performance of Nitinol Stent Designed for Femoral Artery: Finite Element Analysis". English. In: *Journal of Materials Engineering and Performance* 22.11 (2013), pp. 3228–3236. DOI: 10.1007/s11665-013-0635-7.

[35] Anamika Prasad et al. "A computational framework for investigating the positional stability of aortic endografts". English. In: *Biomechanics and Modeling in Mechanobiology* 12.5 (2013), pp. 869–887. DOI: 10.1007/s10237-012-0450-3.

[36] M.L. Raghavan et al. "Wall stress distribution on three-dimensionally reconstructed models of human abdominal aortic aneurysm". In: *Journal of Vascular Surgery* 31.4 (2000), pp. 760–769. DOI: http://dx.doi.org/10.1067/mva.2000.103971.

[37] *Rigid body contact*. Livermore Software Technology Corporation. URL: http://www.dynasupport.com/tutorial/contact-modeling-in-ls-dyna/rigid-body-contact (visited on 01/12/2015).

[38] David Roy et al. "A Literature Review of the Numerical Analysis of Abdominal Aortic Aneurysms Treated with Endovascular Stent Grafts". In: *Computational and Mathematical Methods in Medicine* 2012 (Sept. 2012), pp. 1–16. DOI: 10.1155/2012/820389.

[39] David Roy et al. "Experimental validation of more realistic computer models for stent-graft repair of abdominal aortic aneurysms, including pre-load assess-

ment". In: *International journal for numerical methods in biomedical engineering* 32 (Jan. 2016). DOI: 10.1002/cnm.2769.

[40] Vad S et al. "Determination of coefficient of friction for self-expanding stent-grafts". In: *Journal of biomechanical engineering* 132.12 (2010), p. 121007.

[41] Joel Scott, Darrel Doman, and Clifton Johnston. "Experimental Design for Testing and Analysis of z-Type Self-Expanding Endovascular Stents". In: *International Journal of Biomedical Engineering and Technology* (In-press).

[42] Joel C. R. Scott, Darrel A. Doman, and Clifton R. Johnston. "A Parametric Analysis of Endovascular Stent Geometry Manipulation on Radial Force Performance". In: *Journal of Medical Devices* 14.4 (Oct. 2020). 041004. DOI: 10.1115/1.4048233. eprint: https://asmedigitalcollection.asme.org/medicaldevices/article-pdf/14/4/041004/6570356/med_014_04_041004.pdf.

[43] C. Shu et al. "Endovascular Repair of Complicated Acute Type-B Aortic Dissection with Stentgraft: Early and Mid-term Results". In: *European Journal of Vascular and Endovascular Surgery* 42.4 (2011), pp. 448–453. DOI: http://dx.doi.org/10.1016/j.ejvs.2011.05.013.

[44] Patrick B. Snowhill et al. "Characterization of Radial Forces in Z Stents". In: *Investigative Radiology* 36 (9 Sept. 2001), pp. 521–530.

[45] *SolidWorks*. Dassault Systems. URL: www.solidworks.com (visited on 09/16/2014).

[46] L. Speelman et al. "Initial stress and nonlinear material behavior in patient-specific {AAA} wall stress analysis". In: *Journal of Biomechanics* 42.11 (2009), pp. 1713–1719. DOI: http://dx.doi.org/10.1016/j.jbiomech.2009.04.020.

[47] LS-DYNA Support. *Contact types*. 2001. URL: http://www.dynasupport.com/tutorial/contact-modeling-in-ls-dyna/contact-types (visited on 05/30/2015).

[48] LS-DYNA Support. *How can I handle contact between beams and shells?* URL: http://www.dynasupport.com/faq/contact/how-can-i-handle-contact-between-beams-and-shells (visited on 05/30/2015).

[49] Warren Swee and Michael D Dake. "Endovascular management of thoracic dissections". In: *Circulation* 117.11 (2008), pp. 1460–1473.

[50] Jonathan P Vande Geest et al. "The Effects of Anisotropy on the Stress Analyses of Patient-Specific Abdominal Aortic Aneurysms". In: *Annals of biomedical engineering* 36 (6 June 2008), pp. 921–932. DOI: 10.1007/s10439-008-9490-3.

[51] A.K Venkatasubramaniam et al. "A Comparative Study of Aortic Wall Stress Using Finite Element Analysis for Ruptured and Non-ruptured Abdominal Aortic Aneurysms". In: *European Journal of Vascular and Endovascular Surgery* 28.2 (2004), pp. 168–176. DOI: http://dx.doi.org/10.1016/j.ejvs.2004.03.029.

[52] R. Wang and K. Ravi-Chandar. "Mechanical Response of a Metallic Aortic Stent—Part II: A Beam-on-Elastic Foundation Model". In: *Journal of Applied Mechanics* 71.5 (2004), pp. 706–712. DOI: 10.1115/1.1782912.

[53] Wei Wu et al. "Delivery and release of nitinol stent in carotid artery and their interactions: A finite element analysis". In: *Journal of Biomechanics* 40.13 (2007), pp. 3034–3040. DOI: http://dx.doi.org/10.1016/j.jbiomech.2007.02.024.

[54] Christopher K. Zarins and Charles A. Taylor. "Endovascular Device Design in the Future: Transformation from Trial and Error to Computational Design". In: *Journal of Endovascular Therapy* 16.1 suppl (2009), pp. 12–21. DOI: 10.1583/08-2640.1. eprint: http://jet.sagepub.com/content/16/1_suppl/12.full.pdf+html.

[55] Shijia Zhao, Linxia Gu, and Stacey R. Froemming. "Finite Element Analysis of the Implantation of a Self-Expanding Stent: Impact of Lesion Calcification". In: *Journal of Medical Devices* 6 (2 Apr. 2012), p. 021001.

Appendix A. Convergence Study

Model convergence for this system requires analysis of three separate interacting parts, and therefore has three degrees of freedom. Geometrical refinement of the rollers has made it possible to remove one of the three degrees of freedom in this system. Rollers are modeled as rigid bodies which means there are no stress or strain values calculated for them during the simulation. For stable contacts, rigid bodies require a mesh which accurately captures the true geometry of the part[55]. The length of the tangential, or "sagittal" line between the flat edge created by connecting discretized points on a circular shape, and the arc of the geometric circle is a useful measure of a geometric fit. Figure A2 shows that the roller mesh density of 0.1 mm used in the final model, accurately represents the circular shape being simulated.

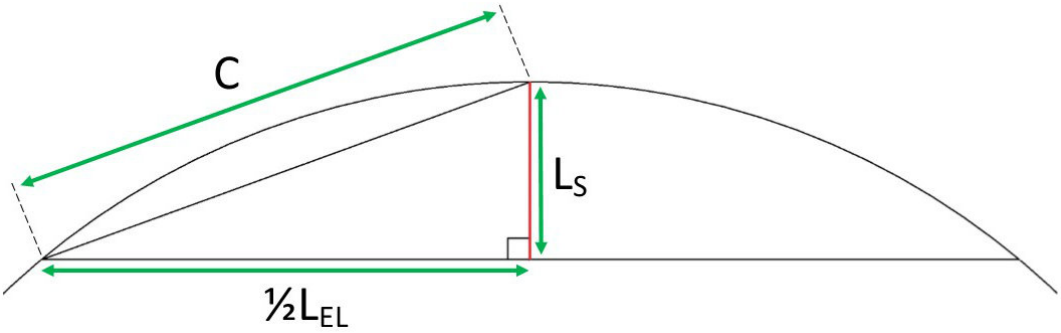

Figure A1. Sagitta line illustration: L_S = sagitta line, L_{EL} = element length, C = strain comparison line

$$C = \sqrt{L_S + \left(\frac{1}{2}L_{EL}\right)^2} \tag{A1}$$

$$\%ErrorStrain = \frac{\frac{1}{2}L_{EL} - C}{C} \tag{A2}$$

where L_S = sagitta line, L_{EL} = element length and C = strain comparison line.

LS-DYNA recommends that rigid body node spacing be no coarser than the mesh of whatever deformable parts it comes into contact with[55]. In the final simulation, the roller mesh size is much smaller than that of the Mylar at 0.1 mm and 0.25 mm respectively. With geometric and mesh density errors minimized, the impact of roller mesh size should not have an impact on overall model convergence or contact stability.

Two degrees of freedom remain, Mylar and stent mesh density, therefore, a two-dimensional convergence study is required to analyze the combined impact of these characteristics on overall model behavior. Convergence is analyzed using both model completion time (Figure A3) and peak simulated force (Figure A4).

The final converged mesh size selection is annotated in Figures A3 and A4 with the letter 'A'. Convergence occurs with a Mylar mesh density of 0.25 mm and a stent

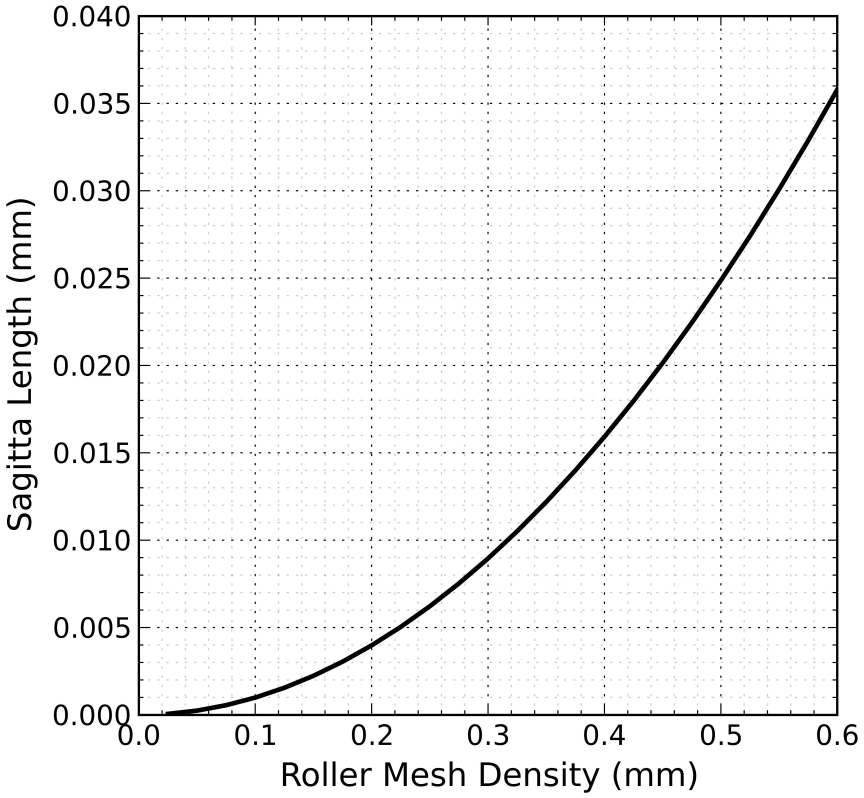

Figure A2. Separation error: a sagitta line drawn between the outer edge of the roller geometry and the mesh created to represent it

mesh density of 0.4 mm. The converged force value of this model is at the center of the convergence "bowl" in Figure A3 at the point which reaches furthest toward equilibrium. Examining the "simulation time" convergence for this same mesh size, point 'A' falls within the equilibrium region of Figure A4, just before a steep ramp up in simulation run-time which occurs with decreasing Mylar mesh density.

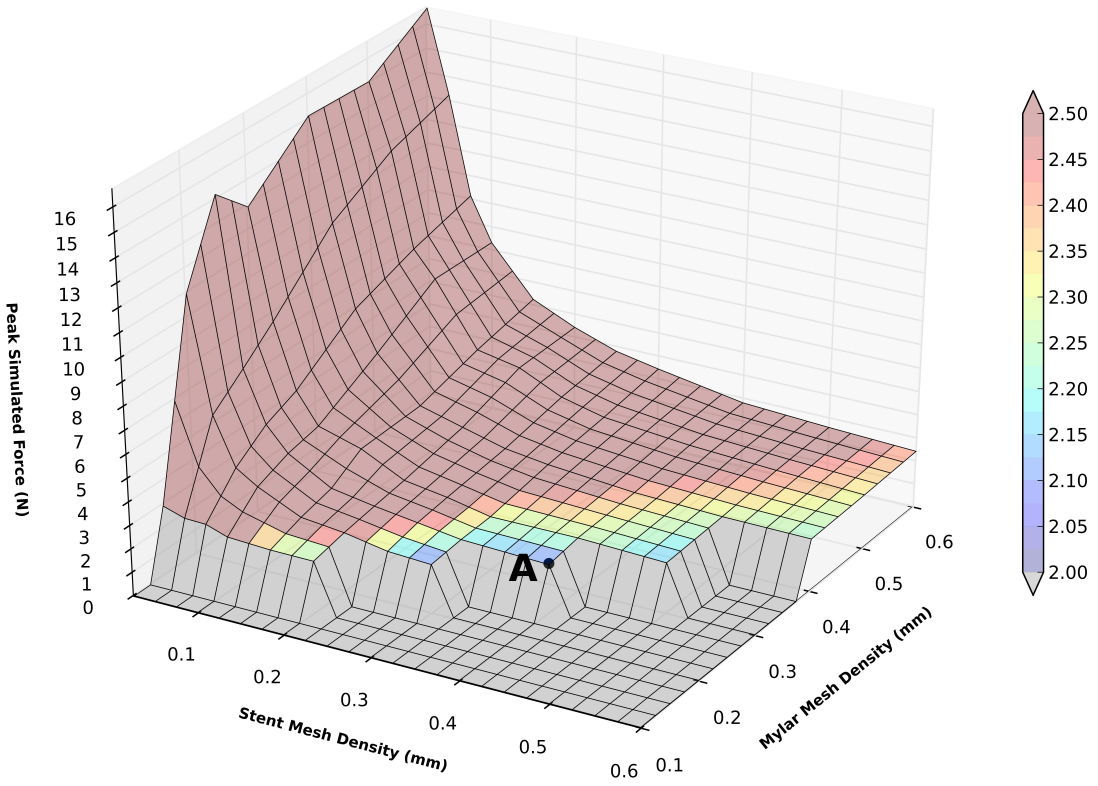

Figure A3. Mesh convergence with respect to peak force

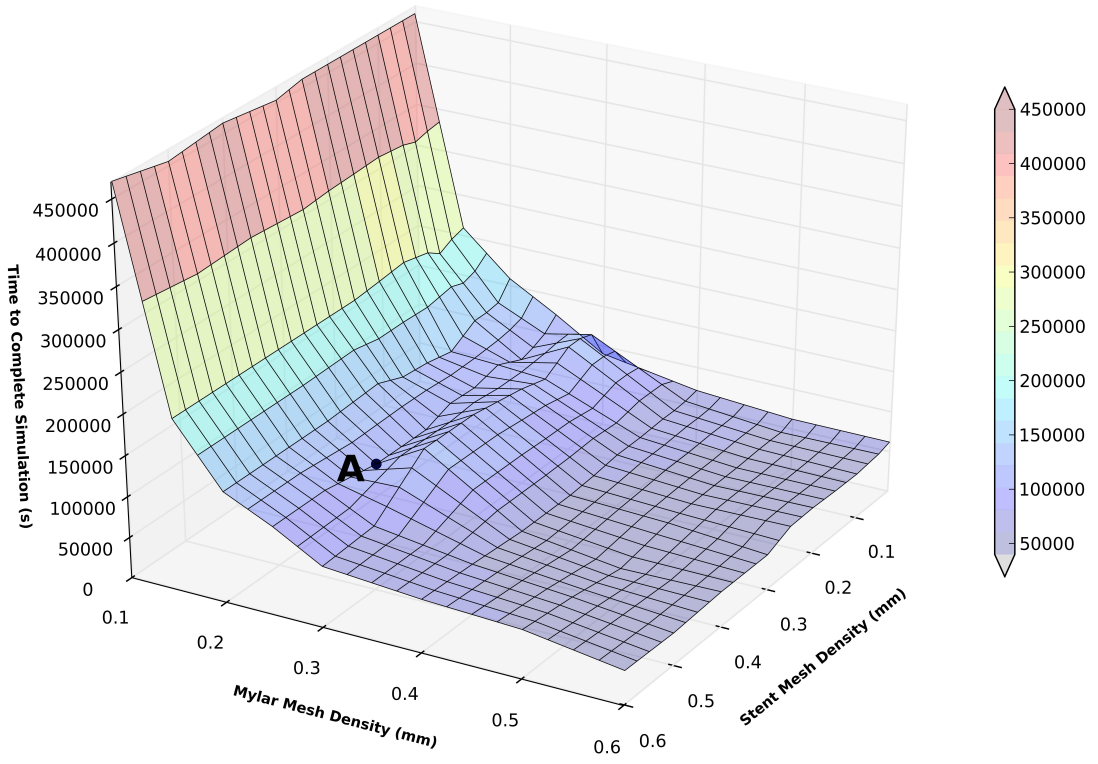

Figure A4. Mesh convergence with respect to simulation duration